Volume 11
Number 15
21 April 2020
Pages 3755–4020

Chemical Science

rsc.li/chemical-science

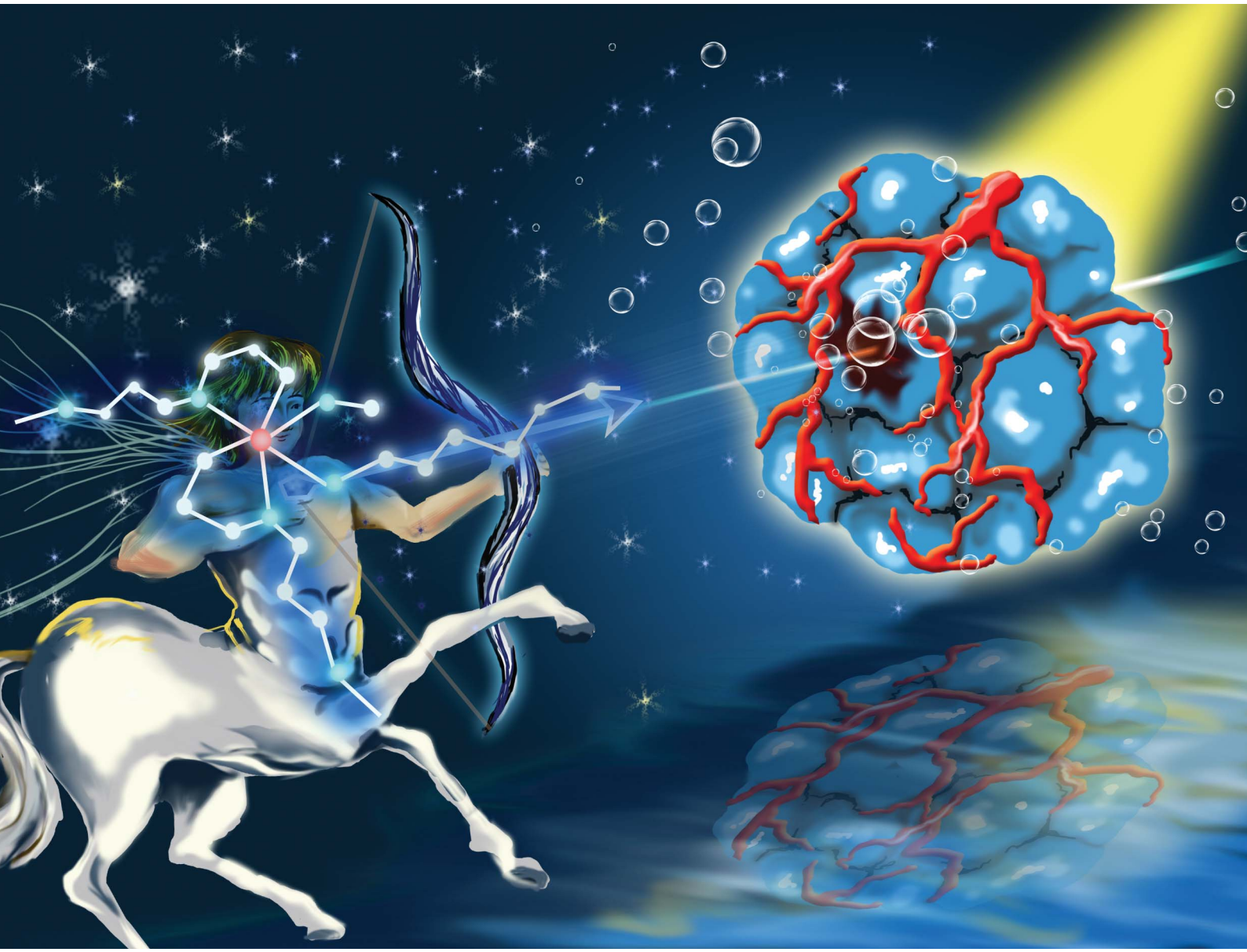

ISSN 2041-6539

ROYAL SOCIETY OF CHEMISTRY

EDGE ARTICLE

Li Ma, Tianfeng Chen *et al.*

A highly X-ray sensitive iridium prodrug for visualized tumor radiochemotherapy

Chemical Science

ROYAL SOCIETY OF CHEMISTRY

EDGE ARTICLE

View Article Online
View Journal | View Issue

Cite this: *Chem. Sci.*, 2020, **11**, 3780

All publication charges for this article have been paid for by the Royal Society of Chemistry

Received 13th February 2020
Accepted 9th March 2020

DOI: 10.1039/d0sc00862a

rsc.li/chemical-science

A highly X-ray sensitive iridium prodrug for visualized tumor radiochemotherapy†

Zhennan Zhao, Pan Gao, Li Ma * and Tianfeng Chen *

Concomitant treatment of radiotherapy and chemotherapy is widely used in cancer therapy. The search for highly efficient radiochemotherapy drugs for tumor targeting therapy under image-guiding is of considerable interest. Herein we report an Ir-based prodrug **Ir-NB** with high sensitization efficiency for *in vivo* tumor microenvironment responsive cancer-targeted bioimaging radiochemotherapy. To the best of our knowledge, the sensitivity enhancement ratio (SER) of the **Ir-NB** prodrug is the highest among those reported for radiotherapy metal complex drugs. From detailed action mechanism study, we provide evidence that the prodrug is effectively suppresses the tumor growth through inducing mitochondrial dysfunction, and eventually amplifies the apoptotic signal pathway. This study provides an approach for the development of cancer theranostic agents for tumor radiotherapy.

Introduction

Chemotherapy has been widely used in cancer therapy concomitantly with radiotherapy or as adjuvant treatment after radiotherapy or surgery.[1–3] The traditional synergistic combination of chemotherapy and radiotherapy normally only reduces the dose of each treatment, while the defects of the two treatments, such as low sensitivity enhancement ratio (SER) and the lack of targeting and visibility, have not been well solved.[1] In order to solve these problems, we have been interested in designing a highly sensitized drug with multifunctional diagnosis and treatment capability to target tumor cells and intelligently respond to the tumor microenvironment (TME). Meanwhile, we would like to employ a chemotherapeutic drug as a potential radiosensitizer (RS) for synergistic sensitization of radiochemotherapy. Based on the above reasons, herein, we report an Ir-based drug **Ir-NB** (Fig. 1a and b) with a SER value of up to 10.35 for visualized tumor radiochemotherapy. To the best of our knowledge, the SER value of **Ir-NB** is the highest among those reported for radiotherapy metal complex drugs (Table S1†).

In order to enhance the efficiency of radiotherapy, materials containing a high atomic number (high-*Z*) element were usually considered as RSs since they can release a large amount of energy in their immediate vicinity through the Auger effect and photoelectric effect when receiving radiation.[4–6] The released large amount of energy was proposed to cause overproduction of reactive oxygen species (ROS) to break the DNA strand and finally induce cell death.[7] Until now, platinum analogues especially cisplatin are the most commonly used agents as RSs and have been proved to target DNA.[8–10] Although RSs targeting DNA can have a lethal effect on cancer cells, they can also pose a threat to genetic stability,[8,11] which hinders their application.

Developing novel organ-targeted, especially mitochondria-targeted RS is a desired way to combat the drawbacks of typical nucleus-targeted RS. Accumulated studies show that the disturbance of mitochondrial function is highly related to radiosensitivity without threatening genetic stability.[12–15] Lipophilic heavy metal complexes (Ir, Ru, *etc.*) with a positive charge are ideal candidates for mitochondria-targeting RSs since heavy metals with high-*Z* are sensitive to X-rays and positively charged materials tend to accumulate in mitochondria.[16,17]

Despite the fact that using lipophilic heavy metal complexes with a positive charge as RSs can well combat the deficiencies of DNA-targeting RSs, the lack of visualization of tumor sites and the low bioavailability of RSs also hinder their application. Cyclometalated iridium-based (Ir, $Z = 77$) materials would be promising candidates for the design of novel RSs with bioimaging function due to their long-lived luminescence, good light stability and also photophysical sensitivity to acidity, oxygen content or viscosity.[18–21] Furthermore, in order to improve the bioavailability of these cyclometalated iridium systems, TME responsive acidity-sensitive imine bonds and lung cancer-targeting functional groups – biotin[22–26] were employed to build an intelligent image-guided radiochemotherapy system.

In this work, we report the design and synthesis of an Ir-based TME-responsive prodrug **Ir-NB** (Fig. 1c) for cancer-targeted bioimaging and radiochemotherapy. From the experimental studies, we provide evidence that upon irradiation, the high atomic number (high-*Z*) Ir(III) complex was localized in

Department of Chemistry, Jinan University, Guangzhou 510632, China. E-mail: tchentf@jnu.edu.cn; chem-mali@foxmail.com

† Electronic supplementary information (ESI) available: Additional figures. See DOI: 10.1039/d0sc00862a

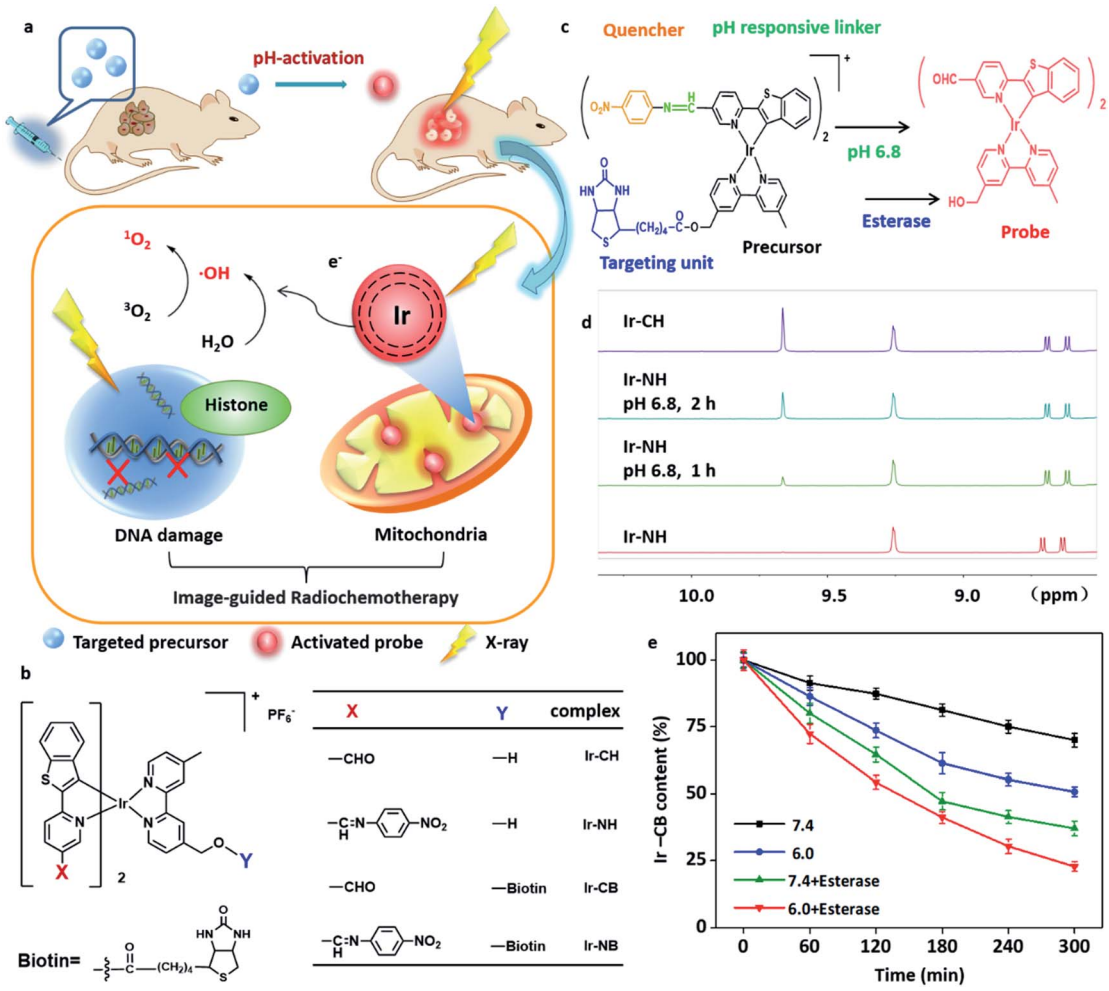

Fig. 1 Bioresponsive process of Ir-based theranostic probes in a tumor microenvironment. (a) Graphical scheme illustrates the conversion of the precursor to the probe upon exposure to acidity and esterase. (b) Chemical structure of Ir(III) complexes in this work. (c) Graphical scheme demonstrates the pH-responsive process of the Ir complex. The probe was activated by acidic conditions and esterase, accompanied by the departure of the quencher and the targeted unit. (d) The pH response of precursor **Ir-NB** in an acidic environment was investigated by ^{1}H NMR. The emerging peak at $\delta = 9.66$ (s) indicated the formation of the aldehyde group of the probe **Ir-CH**. (e) Cumulative drug release of the probe **Ir-CH** from the system through the decomposition of ester in the presence of an acidic environment and esterase as monitored by HPLC.

mitochondria and induced the overproduction of ROS triggering mitochondrial dysfunction, eventually amplifying the apoptotic signal pathway to effectively suppress the tumor growth. This study provides an approach for the development of cancer theranostic agents for tumor radiotherapy.

Results and discussion

Tumor microenvironment responsive process of Ir-based prodrugs

The well-designed targeting image-guided prodrug **Ir-NB** consists of four parts (Fig. 1b and c). The major part is the six coordinated Ir(III) part, which is both a good chemotherapeutic drug and radiotherapy drug, and at the same time, it has strong luminescence emission. In order to accurately visualize the location of tumor sites, the prodrug **Ir-NB** is designed to include another two parts: one is a nitrobenzoyl motif, a strong electron acceptor, which can be used to quench the luminescence emission of the Ir(III) complex owing to the photoinduced electron transfer (PET) process;[18,27] the other one is an acidity-sensitive imine bond, which can be used as a pH responsive linker to be broken in the TME to reproduce the luminescence emission of the Ir(III) complex (Fig. 1c). The last part of **Ir-NB** is a cancer-guiding group to improve the bioavailability of the prodrug. Since lung cancer is the leading cause of cancer death worldwide and with an obvious biotin-receptor, we choose biotin as the guiding group conjugated with the major Ir(III) part through an ester bond.[28] The biotin group can selectively deliver drugs to the lung cancer area followed by ester bond cleavage in the presence of esterase and acidic conditions to release the major Ir(III) part as a RS.[29] The A549 lung carcinoma cell line and WI38 normal lung cell line were choose as models for experiments. Meanwhile, in order to get more insight into this system, Ir-based complexes **Ir-CH** (without cancer-targeting and TME-responsive groups), **Ir-NH** (without cancer-targeting groups) and **Ir-CB** (without TME-responsive groups) were synthesized for comparison (Fig. 1b).

The synthesis of the above-mentioned compounds is explained in Schemes S1 and S2 in the ESI† and the structures were characterized by ESI-TOF MS, CHN elemental analysis, and ^{1}H and ^{13}C NMR spectroscopy. The complexes display absorption bands at 340–520 nm, which could be assigned to metal-to-ligand charge transfer (MLCT) absorption (Fig. S1†). The induction of the nitrobenzoyl moiety causes a blue shift and decline in the emission of the complexes (Fig. S2†), while under acidic conditions the imine bond was disrupted to remove the nitrobenzoyl quencher to release the probe. This was confirmed by ^{1}H NMR (Fig. 1d): by incubation under acidic conditions (pH = 6.8), **Ir-NH** was converted to **Ir-CH** through imine bond disassociation, and a –CHO peak at δ 9.61 in ^{1}H NMR appeared. At the same time, the bioresponse performance of the precursor **Ir-NB** has been further confirmed by incubation in esterase or under acidic conditions. The content of the **Ir-NB** complex was analyzed by high-performance liquid chromatography (HPLC). From the results shown in Fig. 1e, it is found that both esterase and acid treatment contribute to the cleavage of the ester bond. The synergistic effect of acidity and esterase accelerates the unloading process of the biotin unit, and nearly 80% of the conjugates were decomposed under such conditions.

Stimuli signal-amplification process of Ir-based probes

The effective conversion of the precursor to the probe in an acidic environment is beneficial to the tumor diagnostic efficiency, so it's necessary to study in detail the pH-dependent probe response. In order to investigate the pH-induced switch of the probe, we examined the emission spectra of the precursor in the pH range of 5.5–7.8 (Fig. 2a). As the pH decreased, a continuous decline was observed in emission intensity at 580 nm, while a sharp increase was found in the emerging peak at 660 nm. This was suggested to be due to the efficient switch of the precursor to the probe under mildly acidic pH conditions, since the departure of the strongly electron-withdrawing nitrobenzoyl moiety causes the red-shift and enhancement of the emission spectra of the Ir complex. The 3D representations of the fluorescence spectra of the precursor and probe (Fig. 2b and c) suggested that the optimized choices of excitation (>500 nm) and emission (>660 nm) wavelength could eliminate the signal of the precursor during tumor imaging. The pH-induced switch of the probe within cells was also investigated by incubating the A549 cells under different pH conditions. With the decrease of the medium pH (from 7.4 to 6.0), the signal intensity of the probe at 660 nm increases gradually, while the signal strength of the precursor decreases at 580 nm (Fig. 2d). From these experimental results, we can conclude that under neutral conditions (pH = 7.4), the luminescence of **Ir-NB** was quenched due to the PET process from the Ir(III) center to the nitrobenzoyl motif. Under acidic extracellular conditions, the luminescence of **Ir-NB** was enhanced owing to the departure of the nitrobenzoyl motif *via* breaking of the imine bond. These results suggest that the effective conversion of the precursor to the probe in an acidic environment facilitates diagnostic potency in tumors.

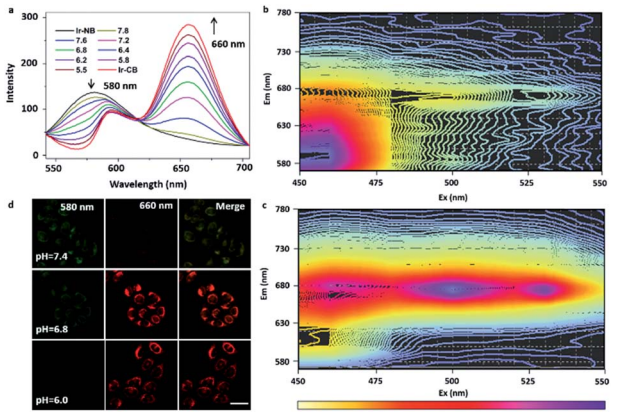

Fig. 2 Stimuli signal-amplification process of the probe in an acidic environment. (a) Emission spectra of the **Ir-NB** after the incubation in solution with different pH values. Three-dimensional representations of the fluorescence spectra of the (b) precursor and (c) probe. Changes in the fluorescence image of cells illustrate the activation of **Ir-NB** under acidic conditions. (d) The A549 cells were incubated with **Ir-NB** (20 μM) in PBS solution at pH 7.4, 6.8 and 6.0 respectively. The labeled cells are observed in the green channel (λ_{ex} = 470, λ_{em} = 570–590 nm) and red channel for the Ir complex (λ_{ex} = 530, λ_{em} = 650–680 nm). Scale bar = 50 μm.

In vitro radiosensitization effect of the Ir-based RSs

In order to evaluate the radiosensitizing activity of the designed drugs, an *in vitro* MTT assay was performed with an X-ray. Prior to evaluating the radiosensitization performance, **Ir-CH** was chosen as the representative to test the stability of the RS. After receiving 8 Gy radiation, no obvious change was found in the HPLC and ^{1}H NMR analysis of **Ir-CH** (Fig. S3†), indicating that the sensitization was ascribed to the intact Ir(III) complex. In addition, the biotin targeting function was evaluated before investigating the radiosensitization performance by using biotin receptor-positive (A549 lung carcinoma cell line) and -negative (WI38 normal lung cell line) cell lines. The biotin-functionalized **Ir-CB** preferentially (Fig. 3a) accumulated in the A549 cells rather than WI38 cells, while the cellular uptake amount of probe **Ir-CH** was almost similar in both cell lines. In addition, excessive biotin pretreatment blocked the uptake of **Ir-CB**, which further confirmed the targeting of biotin receptors. *In vitro* cell experiments showed that the Ir complexes alone had mild toxicity toward A549 and WI38 cells, while the X-ray (4 Gy) cytotoxicity was also not very strong (suppressing A549 cell growth by 14.1%). After combined treatment with the Ir(III) complexes and X-ray radiation, the growth inhibition of A549 cells was enhanced in a dose-dependent manner. Moreover, the targeted RS **Ir-NB** possesses a higher radiosensitization effect than its analogues, which is mainly due to higher intracellular uptake (Fig. 3b). More importantly, the cytotoxic effect of **Ir-NB** (10 μM) combined with X-rays (4 Gy) on A549 cells was much greater than that on WI38 cells (Fig. S4†). In addition, cisplatin, a widely used radiosensitizer, was employed as a positive control to evaluate the radiosensitizing effect of the Ir complexes. The antitumor activity of the synthesized Ir complexes combined with radiotherapy was much higher than that of cisplatin which is widely used in clinics. To further evaluate the interaction between X-rays and Ir RSs, isobologram

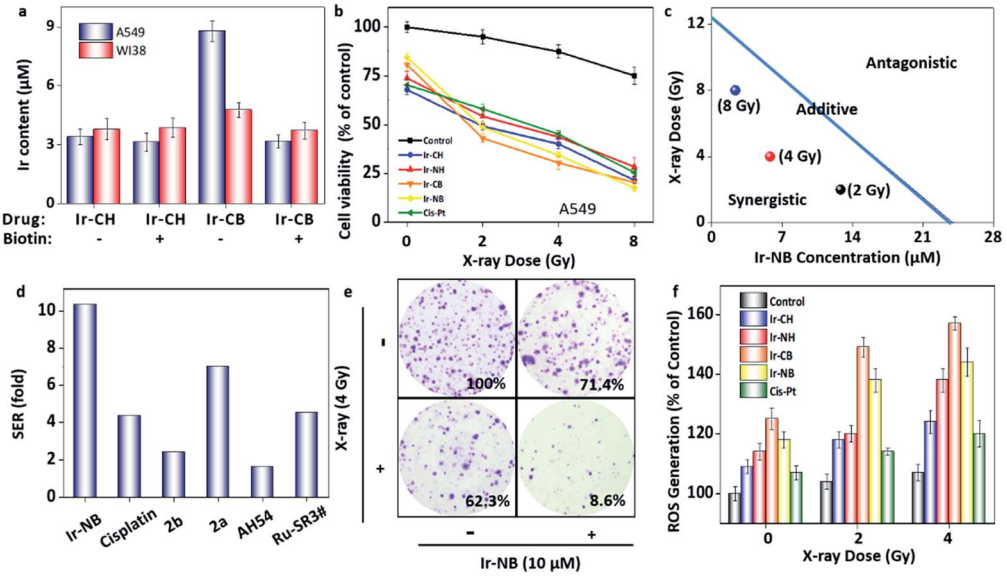

Fig. 3 Iridium-based RSs display a radiosensitization effect in the combined radiochemotherapy. (a) The cellular uptake of the Ir(III) complexes (20 μM) with or without pretreatment with excess biotin (100 μM) by A549 or WI38 cells. (b) Cytotoxic effects of the Ir complexes (10 μM) or cisplatin (10 μM) with/without X-ray irradiation at different dosages on A549 cells. (c) Isobologram analysis of the synergistic antiproliferative effect of combined treatment with X-rays and **Ir-NB** on A549 cells. The data points in the isobologram correspond to the growth inhibition ratio at 50% in the combined treatment. (d) The SER values of different metal-based RSs in this work and previous reports. The details and references are displayed in Table S1 in the ESI.† (e) Representative photographs of the colony formation of A549 cells under co-treatment with the Ir complexes and X-rays for 15 days. The numbers indicate the related colony formation in different groups. (f) Examination of the ROS level of A549 cells after various treatments by using the DCFH-DA probe.

analysis was carried out. As shown in Fig. 3c, the data points in the isobologram are below the line defining the additive effect, indicating that combined treatment with **Ir-NB** and X-rays at different dosages yields a synergistic effect. SER was employed to evaluate the sensitization efficiency of the RSs as displayed in Table S1.† The cancer-targeting Ir-based RSs (SER value under 8 Gy radiation: 10.35 for **Ir-NB** and 10.50 for **Ir-CB**) possess much higher SER than their analogues (SER value under 8 Gy radiation: 6.81 for **Ir-NH** and 6.65 for **Ir-CH**) in the treatment of the A549 cell line, while in the treatment of the WI38 cell line, no obvious difference was found between these four Ir-based RSs. As shown in Fig. 3d, the SER of the designed prodrug **Ir-NB** was much higher than that of cisplatin (SER: 4.36) and other metal-based RSs reported in the literature.[30–34] These results indicated that the cancer-targeting delivery system facilitates the sensitization efficiency of the RS in curing malignant cells. The synergistic effect was further confirmed by the clonogenic survival assay (Fig. 3e and S5a†). Since the radiation at the dosage of 8 Gy obviously suppressed the proliferation of cell lines, radiation dosage at 4 Gy was chosen for further mechanism studies. The survival fractions of A549 cells treated with X-rays (4 Gy) or **Ir-NB** (10 μM) alone are 62.3% and 71.4% respectively, while the combined treatment yielded a synergistic inhibition effect with the survival fraction reduced to 5.6% (Fig. S5b†).

In vitro action mechanism study of the Ir-based RSs

The radiosensitization effect of Ir based RSs motivates us to gain more insight into the action mechanism. Typically, during the radiotherapy, excessive ROS will be generated to induce the breakage of DNA double-strands, so we employed 2′,7′-dichlorofluorescein (DCFH-DA) as a probe to examine the ROS generation from the RS under X-ray irradiation (Fig. 3f). Treatment with the Ir(III) complexes or cisplatin alone slightly increased the ROS level in A549 cells, while the combined treatment with the RSs and X-rays significantly enhanced the intracellular ROS generation, corresponding to the strong tumor growth suppression. After that, we carefully screened whether DNA damage occurred during excessive ROS generation. Phosphorylation of histone H2AX at serine 139 (γH2AX) is the most sensitive marker that can be used to examine the DNA damage.[35] γH2AX can be detected by immunofluorescence using flow cytometric detection to real-time monitor the changes. In our system, the image of immunofluorescence showed that there was no significant change in the expression level of γH2AX soon after **Ir-NB** + X-ray irradiation combined treatment compared with X-ray treatment alone (Fig. 4a), which means that DNA is not the direct target for the excess ROS generation induced by **Ir-NB**. Therefore, we were inspired to investigate the intracellular target of **Ir-NB** by determining the subcellular localization. From the luminescence signal of the probe, we found that the probe was localized in the cytoplasm, which was further verified by the co-staining experiments using a commercial mitochondrion-staining agent (Mito-Tracker Green FM). The results showed that the luminescence signal of the probe (red) and the luminous signal of Mito-Tracker (green) have obvious co-localization, which was reflected by the well-matched yellow area in the merger image,

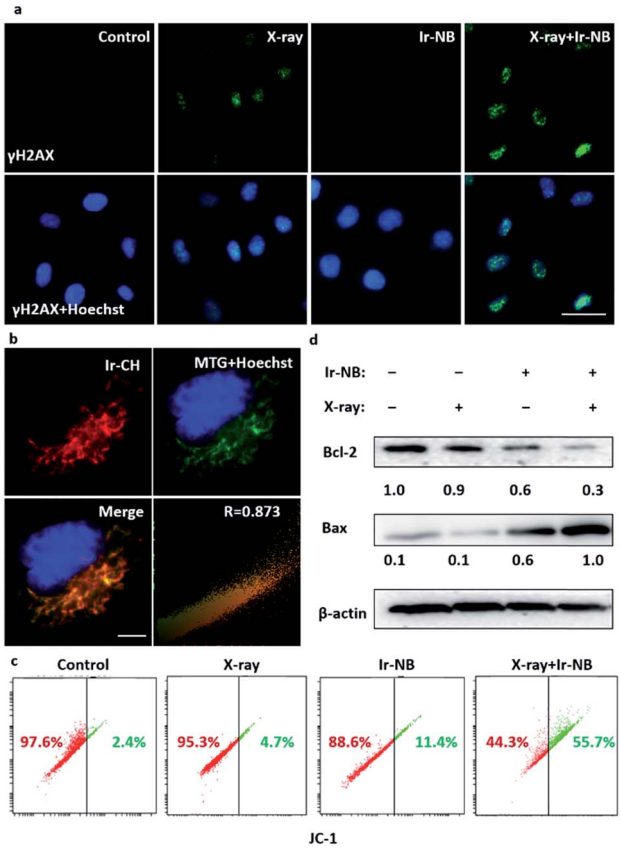

Fig. 4 Mitochondria-targeting iridium RS triggered loss of mitochondrial membrane potentials (MMP) inducing a synergetic effect on anticancer activity. (a) The expression of γH2AX in A549 cells after treatment with **Ir-NB** and X-rays (4 Gy) was visualized using an immunofluorescence stain. Scale bar = 50 μm. (b) Fluorescent image of A549 cells labeled with **Ir-CH** (λ_{ex} = 530, λ_{em} = 650–680 nm), Mito-Tracker green (λ_{ex} = 490, λ_{em} = 510–530 nm) and Hoechst 33324. Scale bar = 10 μm. (c) The loss of mitochondrial membrane potential caused by the X-rays and Ir complex was measured by JC-1 flow cytometric analysis. (d) Expressed levels of Bcl-2 and Bax protein in A549 cancer cells after various treatments, and equal loading was verified by analysis of β-actin in the protein extracts.

and the Pearson's co-localization coefficient at 0.873 (Fig. 4b). On the other hand, the RS **Ir-CH** is highly specific to subcellular mitochondria, revealing that the mitochondria could be a potential target during the radiotherapy. As mentioned, the elevated ROS level of the RS did not significantly promote DNA damage, so we suspect that the mitochondria could be the potential target of the RS considering its subcellular localization. The mitochondrial function is closely related to the radiosensitivity of cancer cells, which motivates us to study the impact of the mitochondrial disturbance on tumor radiosensitivity. Therefore, the mitochondrial membrane potentials (MMP) of A549 cells after radiochemotherapy treatments were measured by using JC-1 flow cytometric analysis. The loss of MMP is accompanied by the shift of JC-1 fluorescence from red to green. As shown in Fig. 4c, only a slight change in MMP was observed when cells were exposed to 4 Gy X-rays or the Ir complex alone. In contrast, cells subjected to combined treatment severely suffered loss of MMP, as reflected by a sharp increase in the population in the defined section of the green fluorescence. These results demonstrate that the combined treatment triggers mitochondrial dysfunction in cancer cells, which is due to the ROS generated by the mitochondria-targeting RS. In order to further confirm the mitochondria-targeting property of the Ir-based RS, Bcl-2 family proteins were detected, since Bcl-2 family proteins can regulate mitochondrial membrane permeability. Therefore, expression levels of pro-survival Bcl-2 protein and pro-apoptotic Bax protein were examined after various treatments. As expected, the Ir(III) complex and combined treatment significantly down-regulated the Bcl-2/Bax expression ratio, while treatment with the X-rays alone has no effect on the expression ratio (Fig. 4d and S6†). Taken together, the radiosensitization effect of the RS can be explained by the following mechanism: the TME-activated Ir(III) complex was preferentially located in the mitochondria that regulate oxidative stress modulation in the rest of the cell. Either treatment with **Ir-NB** alone or combined treatment increases the ratio of Bax/Bcl-2 protein expression, resulting in mitochondrial dysfunction. The dysfunctional mitochondria failed to balance the intracellular oxidative stress, thus increasing radiation sensitivity upon exposure to excess ROS generated during the radiation treatment.[13,36,37] The radiation-induced DNA damage and mitochondria-mediated apoptosis pathway eventually amplify the apoptotic signal pathway to promote cancer cell apoptosis. All these results suggested that the chemotherapeutic and radiosensitization effects of the Ir(III) complexes induce a synergetic effect on suppressing the growth of cancer cells.

In vivo radiosensitization effect of the Ir-NB prodrug

The *in vivo* tumor diagnostic efficacy of Ir-based RSs was evaluated by using A549-inoculated xenograft mice. 12 h after intravenous injection, the targeted functionalized precursor **Ir-NB** was selectively internalized by tumors, accompanied by signal amplification upon exposure to an acidic TME (Fig. 5a). However, the signal of **Ir-CH** diffused throughout the whole body, and **Ir-NH** was unable to accumulate at the tumor site and be activated by the TME. Correspondingly, *ex vivo* luminescence imaging of tumors and main organs (the heart, liver, lungs, spleen, and kidneys) from the sacrificed mice showed that the signal of targeted **Ir-NB** could be selectively detected in the tumors rather than other organs (Fig. 5b). In contrast, the **Ir-CH** and **Ir-NB** tended to be located in the liver. The actual amounts of Ir(III) complexes were further measured by determining the Ir content in tissues (Fig. 5c). We found that the tumor could selectively take up **Ir-NB**, but a considerable amount of Ir content was also observed in the liver in all groups. Despite undesirable biodistribution in the liver, the TME-responsive precursor **Ir-NB** still displayed superior tumor imaging potency, facilitating *in vivo* image guided tumor radiotherapy.

Based on the results of biodistribution, the mice were subjected to X-ray irradiation (2 Gy) 12 h after intravenous (IV) injection with the RS. We found that radiotherapy alone did not effectively suppress tumor growth, and **Ir-NH** mildly inhibited

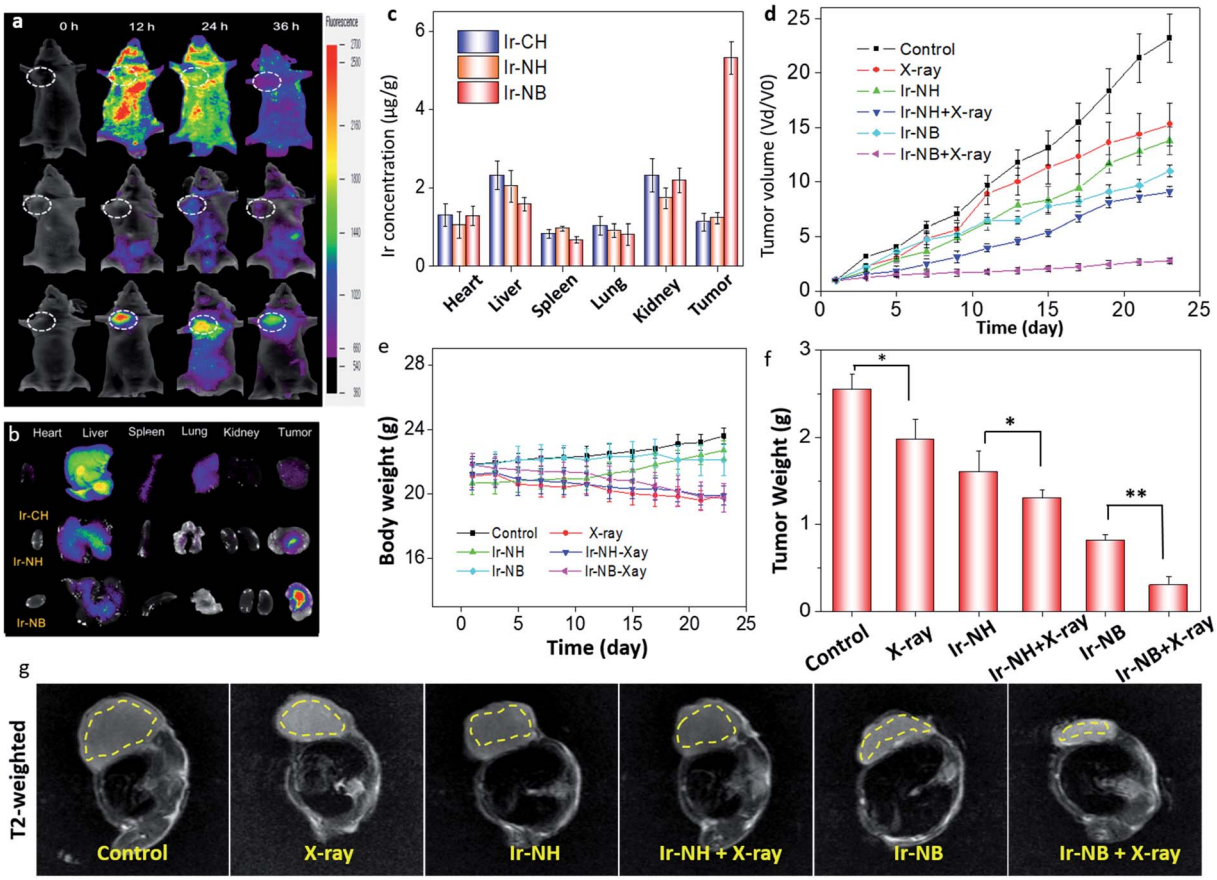

Fig. 5 Image-guided cancer radiochemotherapy of the Ir(III) complexes in xenograft mouse models. (a) Luminescence images of xenograft nude mice after intravenous injection of the Ir complexes (2 μmol kg^{-1}) at different time points. The tumor site was highlighted by the dashed circle. (b) The major organs and tumors were acquired from the sacrificed mice and imaged 36 h after injection of the Ir(III) complexes. (c) The bio-distribution of the Ir complexes was determined by the Ir content in major organs and tumor sites 36 h after injection. The recorded (d) tumor volume, (e) body weight and (f) tumor weight of mice with A549 xenograft after various treatment for 23 days. Each value represents means ± SD ($n = 3$). Bars with different characteristics are statistically different levels *$P < 0.05$, **$P < 0.01$. (g) T_2-Weighted MR images of A549 tumor-bearing mice after different treatments for 23 days. The tumor sites are in the back region and circled by dashed lines.

the growth of tumors (Fig. 5d). Besides the chemotherapeutic effect, **Ir-NB** also possessed favorable radiosensitization ability as reflected by terrific tumor growth suppression (88.6%). Mice treated with X-rays alone suffered loss of body weight without the decrease in tumor weight (Fig. 5e). In contrast, the decrease of body weight in combined treatment groups (**Ir-NH** + X-rays and **Ir-NB** + X-rays) was also accompanied by the decrease in tumor weight (Fig. 5f). The superior radiotherapy sensitization efficacy of **Ir-NB** was ascribed to its favorable biodistribution in tumors.

To profile tissue morphological details, T_2-weighted magnetic resonance (MR) imaging was employed to detect bleeding due to its high spatial resolution in soft tissues. In the T_2-weighted MR experiment, signals can be enhanced by the emergence of tissue edema, and darkening effects will be observed. In the **Ir-NB** and X-ray co-treated group, obvious darkening effects were observed in tumors, while there was only mild change in the T_2-weighted MR signal in the other groups (Fig. 5g). The chemotherapeutic and radiosensitization effects of the Ir(III) complexes induce a synergetic effect on suppressing the growth of tumors *in vivo*, as reflected by the tumor volume of mice calculated using the MR image of the mice (Fig. S7†). Moreover, the slow ADC signal reflects the necrotic degree in the tumor area and blood flow in the tumor vessels. Treatment with the X-rays or Ir complexes alone did not produce an obvious change in the ADC signal compared with the control group (Fig. S8†), while a stronger slow ADC signal in the tumor was detected in the **Ir-NB** + X-ray co-treated group, revealing that **Ir-NB** effectively reduced the cancer cell activity and density compared to **Ir-NH** during the combined treatment.

To assess the systemic toxicity of the RS in the treatment, hematoxylin and eosin (H&E) staining of the main organ and hematological analysis of mice were performed after 23 day treatment. Despite the relatively high levels of the RS accumulating in the liver and spleen, no obvious impairment or inflammation was observed in the main organs compared to the control groups (Fig. 6a). Blood biochemical tests showed that the levels of urea nitrogen (BUN), creatinine (CREA), albumin (ALB), cholesterol (CHOL), lactate dehydrogenase (LDH) and aminotransferase (AST) in the **Ir-NB** + X-ray groups were similar

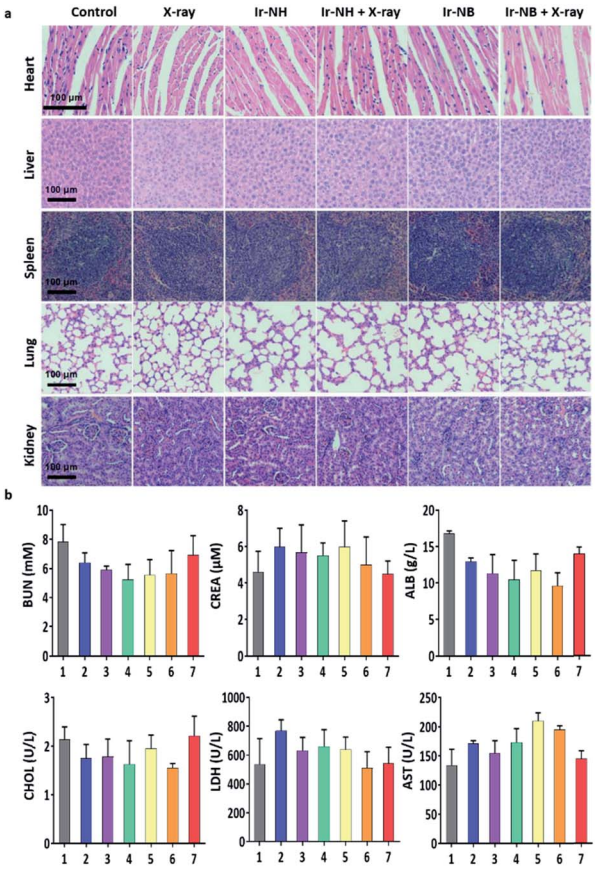

Fig. 6 Systemic toxicity evaluation of the Ir(III) RSs. (a) H&E staining images of the heart, liver, spleen, lung, kidney and tumor from the sacrificed mice after various treatments, scale bar: 100 μm. (b) Hematological analysis of healthy and tumor-bearing nude mice, and those treated with chemoradiotherapy for 23 days. The tested biochemical indexes included blood urea nitrogen (BUN), creatinine (CREA), albumin (ALB), cholesterol (CHOL), lactate dehydrogenase (LDH) and aminotransferase (AST). The numbers represent the group with various treatments: (1) healthy; (2) tumor; (3) X-rays; (4) **Ir-NH**; (5) **Ir-NH** + X-rays; (6) **Ir-NB** and (7) **Ir-NB** + X-rays.

to those of healthy mice (Fig. 6b), demonstrating the safety of the RS in radiotherapy.[38] Based on the experimental results, we concluded that the specific accumulation of **Ir-NB** in tumor sites by drug delivery improves bioavailability and alleviate undesirable side effects of radiotherapy.

Conclusions

In summary, a highly X-ray sensitive novel cancer-targeting Ir(III) complex **Ir-NB** was designed and prepared to act as a RS for realizing image-guided cancer radiochemotherapy. A cancer-targeting unit was conjugated with the RS *via* an ester bond to guide the precursor **Ir-NB** to the TME where the RS was unloaded in such acidic conditions. Meanwhile, the cleavage of the acidity-sensitive imine bond allows the conversion of the precursor to the probe, resulting in enhancement and red shifting in the emission of the activated probe. The activated probe can visualize the tumor site in the mice to allow precise irradiation with X-rays. Besides imaging function, the high-*Z* Ir(III) complex anchored in mitochondria displays chemotherapeutic and radiosensitization potency towards A549 cells owing to the induction of mitochondrial dysfunction. The radiation-induced DNA damage and Ir(III) complex-induced mitochondrial dysfunction eventually amplify the apoptotic signal pathway to promote cancer cell apoptosis. This study provides an approach for the development of cancer radiochemotherapy agents.

Experimental

Materials

Iridium chloride hydrate, ammonium hexafluorophosphate, biotin, selenium dioxide, *N*-hydroxysuccinimide (NHS), and benzo[*b*]thiophen-2-ylboronic acid were obtained from commercial sources and used as received. Tetrakis(-triphenylphosphine)palladium was from Sigma, USA, deuterated solvents were from CIL, USA, and MitoTracker™ Green FM was from Thermo, USA. All other chemicals and materials were used directly without further purification. The antibodies Bcl-2, Bax and phospho-histone H2A.X (Ser139) were purchased from Cell Signaling Technology.

Instruments

^{1}H NMR or ^{13}C NMR spectra of the compounds were obtained using a Bruker ARX 400 NMR spectrometer. The high Performance Liquid Chromatography (HPLC) assay was performed using an Agilent 1260 instrument with 0.5% TFA/H_2O and 0.5% TFA/acetonitrile as eluents. A Hitachi UV-Visible/NIR spectrophotometer UH4150 was used to collect the UV-Vis spectra of the compounds in all experiments. A Thermo Fisher Lumina fluorescence spectrophotometer was employed to record fluorescence spectra. Cell flow cytometry was performed on a BD FACSCanto flow cytometer. The cells and mice radiotherapy experiments were carried out on a PXI X-RAD225 system (Precision X-ray Inc., North Branford, CT) at indicated dosages. The T_2-weighted MR images were collected using a 1.5 T Signa HDxt superconductor clinical MR system (GE medical, Milwaukee, WI, USA). The parameters used are as follows: slice thickness 2.0 mm; TE 82.3 ms; TR 2620 ms; slice spacing 0.2 mm; matrix 256 × 192; and FOV 5 cm × 5 cm.

pH response of the Ir(III) complexes

To investigate the conversion of the precursor to the activated sensor, **Ir-NH** (40 μM) was incubated in PBS solution at different pH values (containing 5% DMSO, ranging from 5.5 to 7.8) at 37 °C for 2 h. The fluorescence spectra of these solutions were collected upon excitation at 490 nm. The three-dimensional representations of the fluorescence spectra of the precursor and sensor were recorded in the PBS solution (pH = 6.8, containing 5% DMSO).

To further profile the pH response of the Ir complex, 10 mg **Ir-NH** was dissolved in 3 mL PBS solution (pH = 6.8, containing 5% DMSO) and incubated at 37 °C for 2 h. The solution was extracted with chloroform, and then the organic layer was

desiccated with magnesium sulfate and evaporated under vacuum. The resultant powder was dissolved in deuterated DMSO before recording the ^{1}H NMR spectrum, which was compared with the spectrum of pure Ir complexes **Ir-CH** and **Ir-NH**.

In vitro release of Ir-CH

The stock solution of **Ir-CB** (final concentration 100 μM) was diluted in four different PBS buffer solutions: (1) pH = 7.4, without esterase; (2) pH = 7.4, with esterase (30 U mL^{-1}); (3) pH = 6.0, without esterase; (4) pH = 6.0, with esterase (30 U mL^{-1}) at 37 °C under continuous stirring. At regular time intervals, 20 μL solution was collected to mix with 180 μL dimethyl sulfoxide to complete the dissolution of drugs. The drug concentration was finally analyzed using a HPLC and detected at 365 nm. A profile shows the residual amount of the Ir-based prodrug after incubation for different times. The experiments were all repeated in triplicate.

Cell culture and cytotoxicity tests

The human lung carcinoma cells (A549) and normal lung fibroblast cells (WI38) were purchased from the American Type Culture Collection (ATCC). The cell lines were cultured using DMEM containing 10% of fetal bovine serum, 100 units per mL of penicillin and 50 units per mL of streptomycin at 37 °C in a humidified incubator with a 5% CO_2 atmosphere. The cells were seeded in a 96-well plate (2×10^3 cells per well) and treated with drugs and/or X-ray irradiation at indicated doses. These cells were exposed to the radiation of X-rays after the incubation of the Ir complexes for 6 h. The cell viability was tested by the MTT assay after the different treatments for 72 h.

Cell fluorescence imaging of the Ir(III) complexes

To examine the pH-activatable property of the Ir complexes, the A549 cells were cultured in a weakly acidic environment as follows. The culture medium of adherent A549 cells was replaced by PBS solutions with different pH values (6.0, 6.8 and 7.4). These cells were incubated with complex **Ir-NB** (10 μM) for 2 h before observation under a microscope.

To investigate intracellular localization of the Ir complexes, the A549 cells were labelled with Mito Tracker Green FM (MTG, Thermo Fishier) according to the product's protocol. The A549 cells were incubated in PBS solution (pH = 6.8) containing 10 μM **Ir-CH** for 2 h and stained with MTG dye, following by observation under a confocal microscope. The fluorescence images were collected in these channels: Hoechst channel (λ_{ex} = 352 nm, λ_{em} = 450–470 nm), MTG channel (λ_{ex} = 460 nm, λ_{em} = 560–600 nm) and **Ir-CH** channel (λ_{ex} = 510 nm, λ_{em} = 670–700 nm).

Intracellular uptake of the Ir(III) complexes

A549 cells or WI38 cells were seeded in a 48-well plate in the presence or absence of extra biotin (100 μM), followed by discarding the medium and supplying fresh medium containing the Ir complexes (20 μM). Then the cells in drug-containing medium were washed using PBS buffer after 2 h incubation. The cells were lysed by adding 200 μL DMSO to release the intracellular Ir complexes. The fluorescence intensity of the Ir complexes was measured using a fluorescence microplate reader (Cytation 5, Bio Tek). The cellular uptake of the Ir complexes was determined by converting the fluorescence intensity into the corresponding concentration of the complex based on a calibrated standard curve.

Colony formation assay

A549 cells (1.2×10^3 cells per well) were cultured in a 6-well plate for 24 h. And then they were treated with the Ir complexes using different dosages for 2 h before irradiation (4 Gy X-rays). After exposure to ionizing radiation, the cells were proliferated for 14 days to allow the formation of the colony. The A549 colony was washed with PBS solution twice and stained with 0.5% crystal violet dye. The labelled samples were finally captured and counted.

Evaluation of mitochondrial membrane potential

The A549 cells were administered with the Ir complex (10 μM) 6 h before X-ray irradiation (4 Gy). After irradiation and 24 h incubation, the A549 cells were harvested and loaded with the JC-1 probe to test the mitochondrial membrane potential (MMP) using a flow cytometer (BD FACSCanto). The percentage of MMP lost was measured by the green fluorescence intensity of JC-1.

Western blot analysis

The change of Bcl-2 and Bax protein expression levels in various treatments was measured by western blotting.[17] After various treatments, the proteins of A549 cells were collected using cell lysis buffer. The proteins were quantified using the BCA protein assay and separated by SDS-PAGE. The protein band and ratio of Bcl-2/Bax expression were calculated using Image J software.

Evaluation of *in vivo* radiotherapy effects of the RS[39]

This study was performed in strict accordance with the national guidelines for the care and use of laboratory animals (Laboratory animal-Guideline for ethical review of animal welfare. GB/T 35892-2018) and was approved by the Animal Experimentation Ethics Committee of Jinan University (Guangzhou, China). Around 1×10^6 cells were injected subcutaneously into female BALB/c nude mice to construct our A549 xenograft model. The model mice were randomly separated into six groups (n = 3) when the tumor volume reached 100 mm^3, and treated by the following steps: (1) saline, (2) saline and X-rays, (3) **Ir-NH**, (4) **Ir-NH** and X-rays, (5) **Ir-NB**, (6) **Ir-NB** and X-rays. The mice were intravenously injected with saline containing the Ir(III) complexes (2 μmol kg^{-1}) every 2 days for 23 days. Afterwards, the mice were subjected to X-ray irradiation at a dosage of 2 Gy 12 h after injection. The tumor volume was measured every other day, and obtained by the equation: volume (mm^3) = $l \times w^2/2$, where l is the maximal length and w is the width of the tumor. At the end of treatments, the T_2-weighted MR images

and slow ADCs of the mice were captured using a 3.0-TMR scanner (General Electric, Milwaukee, WI, USA). The mice were sacrificed to collect the blood sample and the organs for the evaluation of systemic toxicity. The blood sample was analysed by hematology. Tissue samples were digested to measure the Ir content using ICP-AES analysis to obtain the biodistribution.

In vivo and *ex vivo* luminescence imaging

The fluorescence of the Ir complexes was collected using a FOBI Bio-Imaging system. For the *in vivo* experiment, A549 xenograft nude mice were intravenously treated with Ir(III) complex (2 μmol kg^{-1}) injection, followed by anesthetizing the mice and observing them using the imaging system at various time points (0, 12, 24 and 36 h). After 36 h observation, the mice were sacrificed to collect the tissues and tumors for *ex vivo* fluorescence analysis. Fluorescence filter settings were employed in fluorescent imaging (ex/em: 500/680 nm).

Statistical analysis

All data were collected in at least triplicate and represented as means ± SD. Differences between two groups were examined by the two-tailed Student's *t* test. Significant differences were noted with asterisks as $P < 0.05$ (*) or $P < 0.01$ (**).

Conflicts of interest

There are no conflicts to declare.

Acknowledgements

This work was supported by the Natural Science Foundation of China (21877049 and 21701054), Major Program for Tackling Key Problems of Industrial Technology in Guangzhou (201902020013), Pearl River Nova Program of Guangzhou (201906010077), and Dedicated Fund for Promoting High-Quality Marine Economic Development in Guangdong Province (GDOE-2019-A31).

References

1 J. Bourhis, C. Sire, P. Graff, V. Gregoire, P. Maingon, G. Calais, B. Gery, L. Martin, M. Alfonsi, P. Desprez, T. Pignon, E. Bardet, M. Rives, L. Geoffrois, N. Daly-Schveitzer, S. Sen, C. Tuchais, O. Dupuis, S. Guerif, M. Lapeyre, V. Favrel, M. Hamoir, A. Lusinchi, S. Temam, A. Pinna, Y. G. Tao, P. Blanchard and A. Auperin, *Lancet Oncol.*, 2012, **13**, 145–153.
2 H. Y. Deng, W. P. Wang, Y. C. Wang, W. P. Hu, P. Z. Ni, Y. D. Lin and L. Q. Chen, *Eur. J. Cardiothorac. Surg.*, 2017, **51**, 421–431.
3 T. Y. Seiwert, J. K. Salama and E. E. Vokes, *Nat. Clin. Pract. Oncol.*, 2007, **4**, 86–100.
4 Y. Yong, C. Zhang, Z. Gu, J. Du, Z. Guo, X. Dong, J. Xie, G. Zhang, X. Liu and Y. Zhao, *ACS Nano*, 2017, **11**, 7164–7176.
5 H. Liu, W. Lin, L. He and T. Chen, *Biomaterials*, 2020, **226**, 119545.
6 Y. Duo, Y. Huang, W. Liang, R. Yuan, Y. Li, T. Chen and H. Zhang, *Adv. Funct. Mater.*, 2020, **30**, 1906010.
7 Y. Li, K. H. Yun, H. Lee, S. H. Goh, Y. G. Suh and Y. Choi, *Biomaterials*, 2019, **197**, 12–19.
8 S. Corde, J. Balosso, H. Elleaume, M. Renier, A. Joubert, M. C. Biston, J. F. Adam, A. M. Charvet, T. Brochard, J. F. Le Bas, F. Esteve and N. Foray, *Cancer Res.*, 2003, **63**, 3221–3227.
9 M. C. Biston, A. Joubert, J. F. Adam, H. Elleaume, S. Bohic, A. M. Charvet, F. Esteve, N. Foray and J. Balosso, *Cancer Res.*, 2004, **64**, 2317–2323.
10 Y. Altundal, G. Cifter, A. Detappe, E. Sajo, P. Tsiamas, P. Zygmanski, R. Berbeco, R. A. Cormack, M. Makrigiorgos and W. Ngwa, *Phys. Med.*, 2015, **31**, 25–30.
11 J. S. Bertram, *Mol. Aspects Med.*, 2000, **21**, 167–223.
12 Y. Kaneyuki, H. Yoshino and I. Kashiwakura, *J. Radiat. Res.*, 2012, **53**, 145–150.
13 S. Anoopkumar-Dukie, T. Conere, G. D. Sisk and A. Allshire, *Br. J. Radiol.*, 2009, **82**, 847–854.
14 K. Y. Ni, G. X. Lan, S. S. Veroneau, X. P. Duan, Y. Song and W. B. Lin, *Nat. Commun.*, 2018, **9**, 4321–4334.
15 C. Y. Yu, H. Xu, S. Ji, R. T. Kwok, J. W. Lam, X. Li, S. Krishnan, D. Ding and B. Z. Tang, *Adv. Mater.*, 2017, **29**, 1606167–1606176.
16 J. Liu, H. Lai, Z. Xiong, B. Chen and T. Chen, *Chem. Commun.*, 2019, **55**, 9904–9914.
17 Z. Zhao, P. Gao, Y. You and T. Chen, *Chem.–Eur. J.*, 2018, **24**, 3289–3298.
18 W. Wu, R. Guan, X. Liao, X. Yan, T. W. Rees, L. Ji and H. Chao, *Anal. Chem.*, 2019, **91**, 10266–10272.
19 X. Zheng, H. Mao, D. Huo, W. Wu, B. Liu and X. Jiang, *Nat. Biomed. Eng.*, 2017, **1**, 57–65.
20 W. Lv, Z. Zhang, K. Y. Zhang, H. R. Yang, S. J. Liu, A. Q. Xu, S. Guo, Q. Zhao and W. Huang, *Angew. Chem., Int. Ed.*, 2016, **55**, 9947–9951.
21 L. Hao, Z. W. Li, D. Y. Zhang, L. He, W. T. Liu, J. Yang, C. P. Tan, L. N. Ji and Z. W. Mao, *Chem. Sci.*, 2019, **10**, 1285–1293.
22 Z. Song, Y. Chang, H. Xie, X. F. Yu, P. K. Chu and T. Chen, *NPG Asia Mater.*, 2017, **9**, e439.
23 Y. Chang, L. He, Z. Li, L. Zeng, Z. Song, P. Li, L. Chan, Y. You, X. F. Yu, P. K. Chu and T. Chen, *ACS Nano*, 2017, **11**, 4848–4858.
24 L. Chan, P. Gao, W. Zhou, C. Mei, Y. Huang, X. F. Yu, P. K. Chu and T. Chen, *ACS Nano*, 2018, **12**, 12401–12415.
25 Z. Zhao, X. Zhang, C. E. Li and T. Chen, *Biomaterials*, 2019, **192**, 579–589.
26 Y. Huang, Y. Fu, M. Li, D. Jiang, C. J. Kutyreff, J. W. Engle, X. Lan, W. Cai and T. Chen, *Angew. Chem., Int. Ed.*, 2020, **59**, 4406–4414.
27 C. L. Liu, R. Zhang, W. Z. Zhang, J. P. Liu, Y. L. Wang, Z. B. Du, B. Song, Z. P. Xu and J. L. Yuan, *J. Am. Chem. Soc.*, 2019, **141**, 8462–8472.
28 R. Kumar, J. Han, H. J. Lim, W. X. Ren, J. Y. Lim, J. H. Kim and J. S. Kim, *J. Am. Chem. Soc.*, 2014, **136**, 17836–17843.
29 X. Wang, X. Feng, G. Ma, L. Yao and M. Ge, *Adv. Mater.*, 2016, **28**, 3131–3137.

30 Z. Deng, L. Yu, W. Cao, W. Zheng and T. Chen, *Chem. Commun.*, 2015, **51**, 2637–2640.
31 Z. Q. Deng, L. L. Yu, W. Q. Cao, W. J. Zheng and T. F. Chen, *ChemMedChem*, 2015, **10**, 991–998.
32 Q. Xie, G. Lan, Y. Zhou, J. Huang, Y. Liang, W. Zheng, X. Fu, C. Fan and T. Chen, *Cancer Lett.*, 2014, **354**, 58–67.
33 Y. Zhou, Y. Xu, L. Lu, J. Ni, J. Nie, J. Cao, Y. Jiao and Q. Zhang, *Theranostics*, 2019, **9**, 6665–6675.
34 R. Carter, A. Westhorpe, M. J. Romero, A. Habtemariam, C. R. Gallevo, Y. Bark, N. Menezes, P. J. Sadler and R. A. Sharma, *Sci. Rep.*, 2016, **6**, 20596.
35 H. Zhao, X. Huang, H. D. Halicka and Z. Darzynkiewicz, *Curr. Protoc. Cytom.*, 2019, **89**, e55.
36 R. Kim, H. Inoue and T. Toge, *Int. J. Mol. Med.*, 2004, **14**, 697–706.
37 W. O. Arafat, J. Gomez-Navarro, J. Xiang, M. N. Barnes, P. Mahasreshti, R. D. Alvarez, G. P. Siegal, A. O. Badib, D. Buchsbaum, D. T. Curiel and M. A. Stackhouse, *Mol. Ther.*, 2000, **1**, 545–554.
38 L. Zheng, C. Li, X. Huang, X. Lin, W. Lin, F. Yang and T. Chen, *Biomaterials*, 2019, **216**, 119220–119230.
39 C. Dai, L. He, B. Ma and T. Chen, *Small*, 2019, **15**, e1902642.